THERMAL CONDUCTIVITY OF THIN FILM NIOBIUM DISELENIDE FROM TEMPERATURE-DEPENDENT RAMAN

A Thesis

Presented to the Faculty of the Graduate School

of Cornell University

in Partial Fulfillment of the Requirements for the Degree of

M.S

by

Huai-Hsun Lien

August 2017

ABSTRACT

Niobium diselenide ($NbSe_2$) possess a high electrical conductivity and low thermal conductivity, making it a candidate for thermoelectric devices. While the electronic properties of $NbSe_2$ has been relatively explored, the lateral thermal conductivity for $NbSe_2$ has remained unknown. In this report, we present the lateral thermal conductivity of $NbSe_2$ determined by nondestructive opto-thermo method utilizing micro-Raman spectroscopy. The thermal conductivity $\kappa = (15 \pm 4)$ W/mK was obtained at room temperature and we further verified by hall measurements that $NbSe_2$ conducts heat mostly through electrons. The results shed lights on the potential of Niobium diselenide as a thermoelectric device.

BIOGRAPHICAL SKETCH

EDUCATION

Master of Science in Materials Science and Engineering

College of Engineering, Cornell University Ithaca, N.Y Cumulative GPA: 3.98

Bachelor of Science in Materials Science and Engineering

College of Science and Engineering, National Tsing Hua University (NTHU) Hsinchu, Taiwan GPA: 3.96

RESEARCH and PROJECT EXPERIENCE

Masters Student, Cornell University, Ithaca, N.Y Aug. 2015 to present

Project: Thermal conductivity of thin film $NbSe_2$ using temperature-dependent Raman spectroscopy

PVD Intern, GLOBALFOUNDRIES, Malta, N.Y Jun. 2016 to Aug. 2016

Project: The effectiveness of qual wafers for tool-chamber health monitoring

TEACHING and EXTRACURRICULAR EXPERIENCE

Teaching assistant, NTHU, Hsinchu, Taiwan Sept. 2012 to Jun. 2013

Courses: Introduction to quantum physics, Introduction to transport phenomena, Mechanical properties, Physical properties of materials, Diffusion and phase transformation

For my parents.

ACKNOWLEDGEMENTS

I would like to thank my thesis advisor, Prof. Debdeep Jena and Prof. Grace Xing for this opportunity to work in their group and experience the world of scientific research. They have been good mentors and their continuous guidance is invaluable, without them this thesis would have been impossible. I would also like to thank Dr. Rusen Yan for his pioneering work in this field, his comments and advice have helped me throughout this project. Special thanks to Suresh Vishwanath as my mentor, I am grateful for all the trainings and assistance.

I would like to thank the staff at CCMR for the assistance, especially Prof. Kit Umbach, Philip Carubia, and Dr. Maura Weathers for their constant assistance. I would also like to thank the staff at CNF especially Amrita Banerjee. I would like to give big thanks to Dr. Vladimir Protasenko, our lab manager for helping me with my project. I would also like to thank our collaborators, Prof. Tengfei Luo and Prof. Morten Eskildsen at Notre Dame, Prof. Libai Huang at Purdue.

Lastly, I would like to thank the big Jena Xing group members for your continuous support, Kazuki, Henryk, Yongjin, Moudud, Zhongyan, Mingda Lee, Mingda Zhu, Alex, Brian, Jimy, Kevin, Shyam, Wenshen, Nick, Sam, Reet, Austin, Xiang, Joe, Hyunjea, John, Jae Ho, especially Liheng Jerry Zhang and Aditya Sunder.

TABLE OF CONTENTS

Biographical Sketch . . . iii
Dedication . . . iv
Acknowledgements . . . v
Table of Contents . . . vi
List of Tables . . . vii
List of Figures . . . viii

1 Introduction **1**
1.1 Niobium Diselenide and it's challenge . . . 1
1.2 Overview of this thesis . . . 1

2 Literature review on temperature-dependent Raman **3**
2.1 Silicon . . . 3
2.2 Graphene . . . 4
2.3 Transitional metal dichaclogenides . . . 5
2.3.1 MoS_2 . . . 6
2.3.2 $MoSe_2$ . . . 6
2.3.3 WS_2 . . . 7

3 Heat diffusion model **8**
3.1 Boundary conditions and coefficients . . . 9
3.2 Parameters . . . 13
3.2.1 Half Guassian beam width r_0 . . . 14
3.2.2 Absorption coefficient α . . . 18
3.2.3 Interfacial thermal conductance g . . . 19
3.2.4 Supported thermal conductivity κ_s . . . 20

4 Temperature- and power-dependent Raman **23**
4.1 Sample preparation . . . 23
4.1.1 Surface roughness and flake thickness . . . 25
4.2 Measurement setup . . . 26
4.2.1 Raman system . . . 27
4.2.2 Cryostat . . . 27
4.2.3 Absorption coefficient . . . 28
4.3 Results . . . 30
4.3.1 Temperature-dependent Raman . . . 31
4.3.2 Power-dependent Raman . . . 35

5 Hall measurement **39**

A Additional Power-dependent measurement **40**

Bibliography **45**

LIST OF TABLES

4.1 First-order temperature coefficient 34
4.2 First-order power coefficient 36
4.3 Extracted κ using different χ_T and χ_P 36

A.1 First-order power coefficient 40

LIST OF FIGURES

3.1 Example stacking of $T(r)$ for different κ. 11
3.2 Example stacking of $T(r)$ and $q(r)$ plot. 12
3.3 Visualization of T_m calculation. 13
3.4 $q(r)$ for 100X NA=0.9 lens 15
3.5 $q(r)$ for 50X NA=0.75 lens. 15
3.6 $q(r)$ for long-working distance 50X NA=0.65 lens. 16
3.7 $q(r)$ stacking for 100X, 50X, and LW 50X lens. 16
3.8 κ for various r_0 using A_{1g}. 17
3.9 κ for various r_0 using E^1_{2g}. 17
3.10 κ for various α using A_{1g}. 18
3.11 κ for various α using E^1_{2g}. 18
3.12 $T(r)$ for various g using κ = 15 W/mK. 19
3.13 Extracted κ for various g, A_{1g} mode. 20
3.14 Extracted κ for various g, E^1_{2g} mode. 20
3.15 $T(r)$ for various κ_s to κ ratio. 21
3.16 Extracted κ for various κ_s to κ ratio, A_{1g} mode. 21
3.17 Extracted κ for various κ_s to κ ratio, E^1_{2g} mode. 22

4.1 Optical image of 161027_HL_NbSe_2 and 170117_HL_NbSe_2. 24
4.2 AFM image of 161027_HL_NbSe_2 for temperature-dependent Raman. 24
4.3 Step height of 161027_HL_NbSe_2, the sample is measured to be 25 nm. 24
4.4 AFM image of 170117_HL_NbSe_2 for power-dependent Raman. . 25
4.5 Step height of 170117_HL_NbSe_2, the sample is measured to be 120 nm. 25
4.6 The RMS for the linear trench is measured to be 0.9 nm. 26
4.7 The RMS for the circular trench is measured to be 4.16 nm. 26
4.8 Schematic drawing of absorption measurement, the value in the box indicate the percentage measured at the terminal. The value measured before the light blue lens (red box) is set as the initial value. 28
4.9 The transmission percentage of each individual component. The transmission of the beam splitter (light green) and the lens (gray) are used. 29
4.10 The calibration measurement using Si with 200 μm SiO_2, the values in the boxes are absolute values measured. 29
4.11 The absorption measurement data of 100nm $NbSe_2$ sample. . . . 30
4.12 Example Lorentzian fitting. 31
4.13 Example Lorentzian fitting for 110 K, 180 K, 270 K, and 340 K. . . 32
4.14 Raman shift of 25 nm and 20nm $NbSe_2$ with respect to temperature using linear trench. 33

4.15 FWHM for 161027_*HL_NbSe*2 with respect to temperature, the FWHM of A_{1g} mode increases after 250K while no trend observed for E^1_{2g} mode. 34
4.16 Example Lorentzian fitting for 0.317 mW, 0.347 mW, 0.384 mW, and 1.024 mW. 35
4.17 Raman shift of 120nm $NbSe_2$ with respect to power using circular trench. 36
4.18 κ difference resulting from Gaussian beam width deviation using A_{1g} mode. 37
4.19 κ difference resulting from Gaussian beam width deviation using E^1_{2g} mode. 38

5.1 From the left, 100× optical image of $NbSe_2$ on prepatterned Hall bar substrate. Dotted lines show the Hall bar patterned, both width and length are 2 μm. 39

A.1 κ obtained from various measurements for power-dependent Raman.Sample *161208* and *170228* does not have full coverage over the trench. 40
A.2 Raman shift of 161208_*HL_NbSe*$_2$ (100nm) with respect to power using circular trench. 41
A.3 Raman shift of 161208_*HL_NbSe*$_2$ (80nm) with respect to power using circular trench. 41
A.4 AFM image of 161208_*HL_NbSe*$_2$ (100nm). 42
A.5 Step height of 161208_*HL_NbSe*$_2$, the sample is measured to be 100 nm. Note that the trench is not fully covered. 42
A.6 AFM image of 170227_*HL_NbSe*$_2$ (80nm). 43
A.7 Step height of 170227_*HL_NbSe*$_2$, the sample is measured to be 80 nm. Note that the trench is not fully covered. 43
A.8 AFM image of 161020_*HL_NbSe*2 (20nm). Another sample for temperature-dependent Raman. 44
A.9 Step height of 161020_*HL_NbSe*2, the sample is measured to be 20 nm. 44

CHAPTER 1

INTRODUCTION

The discovery of graphene[1] and the mechanically exfoliation technique have led to many advancements in layered materials. Layered materials are bounded by van der Waals force, which give rise their unique properties. The absence of dangling bonds at the surface enables them to grow defect free heterostructures by van der Waals epitaxy[2]. The properties of mono- to few-layer materials, however, have remained relatively unexplored. With the progressing of mechanically exfoliation techniques, we are able to fabricate samples and explore their unique properties.

1.1 Niobium Diselenide and it's challenge

Early studies of $NbSe_2$ demonstrated $NbSe_2$ to be among the first few layered-structured superconductors with T_c ranging from 5.9 to 7.0 K[3]. About the same time, bulk thermoelectric properties studies[4] of $NbSe_2$ showed Seebeck coefficient of 12 (μV/K) and the thermal conductivity of 2.1 (W/mK). $NbSe_2$ is a sensitive materials that oxidizes easily under open environment, therefore determining the thermal conductivity of thin film $NbSe_2$ is non-trivial.

1.2 Overview of this thesis

Recent studies on TMDs (transitional metal dichalcogenindes) have shown dissimilar and unique properties that is absent in their bulk form [5]. The challenge

in determining the thermal conductivity of thin film $NbSe_2$ lies in the material's tendency of oxidation in ambient environment. However, by utilizing the contactless opto-themo method we eliminate this concern by enclosing the thin film $NbSe_2$ sample in vacuum environment. The result is $\kappa = (15 \pm 4)$ W/mK. We also performed Hall measurements to determine the electron contribution of the thermal conductivity. Measurements ranging from 1 μA to 500 μA returns average resistance of 3.09×10^{-7} Ωm, corresponding to electron thermal conductivity κ_e of 23.9 W/mK by WiedemannFranz law. The κ is extracted using radial heat diffusion model by fitting the increase in sample temperature to experimental obtained results.

CHAPTER 2

LITERATURE REVIEW ON TEMPERATURE-DEPENDENT RAMAN

In this chapter includes a brief review of the past results using temperature-dependent Raman. Several advantages of this method are: non-destructive, contactless, quick response, and relatively resistant to crystal impurities. Temperature-dependent Raman was first employed on silicon before moving on to other materials. A detailed review of determining κ using this technique is provided by Judek[6]. The purpose of this review is to provide readers a compact and general knowledge of this technique.

2.1 Silicon

The study of the decaying of optical phonon to two LA phonon in silicon[7] were the very first studies utilizing temperature-dependent Raman. They observed temperature dependence for both the Raman frequency and linewidth. The use of temperature-dependent Raman to determine κ, however, were first used for silicon with different porosity[8]. In the report, they employed laser beam heating which will cause the local temperature to rise and the increase in local temperature is largely dependent on the local κ. The relation of local κ can be described as

$$\kappa = \frac{2\Delta P}{\pi a \Delta T} \tag{2.1}$$

where πa is the beam periphery. $\Delta P = P_2 - P_1$ is the power difference and $\Delta T = T_2 - T_1$ is the temperature increase. Both T_1 and T_2 are predetermined by temperature-dependent Raman which the laser power is set to the lowest laser power to minimize the heating of the sample. This report established the

use of temperature-dependent Raman to determine the local heat increment. This method turns out to be very powerful that later it led to the opto-thermal technique which is currently used to extract the κ of thin films.

2.2 Graphene

Temperature dependence of graphene were first reported by Calizo et at.[9] They observed the Raman frequency shift of G mode for both bi- and monolayer graphene. The frequency of the G mode with respect to temperature can be fitted by

$$\omega = \omega_0 + \chi_T T \tag{2.2}$$

where ω_0 is the G mode frequency when temperature T approaches 0 K with a linear extrapolation. χ_T is the first-order temperature coefficient. The higher-order terms were ignored because they are expected to appear at higher temperature[10]. The Raman frequency shift due to temperature can be described by thermal expansion and other anharmonic effect which can be observed in silicon[7]. Later, Balandin et al.[11] restrict the heat flow within graphene by suspending the flake over a trench. With the energy conservation equation he obtained

$$\frac{\partial Q}{\partial t} = -\kappa \oint \nabla T \cdot dS \tag{2.3}$$

where Q is the heat transfer within time t. He considered two limiting cases, for the radial heat wave

$$\kappa = \chi_T \frac{1}{2h\pi} \Big(\frac{\delta\omega}{\delta P} \Big)^{-1} \tag{2.4}$$

where $\frac{\delta\omega}{\delta P}$ is the Raman peak position shift of G mode due to power difference and h is the thickness of monolayer graphene. Another extreme case he consid-

ered is the plane-wave heat front

$$\kappa = \chi_T \frac{L}{2hW}\Big(\frac{\delta\omega}{\delta P}\Big)^{-1} \tag{2.5}$$

where L and W is the length and width of the flake. With the above equations he was able to extract the suspended κ for graphene to be $(4.84 \pm 0.44) \times 10^3$ to $(5.3 \pm 0.48) \times 10^3$ W/mK. This is the first reported thermal conductivity for graphene, however, the values were an overestimate.

Cai et al.[12] refined the technique by growing graphene on top of Au-coated SiN_x membrane with 3.8 μm holes. With the introduction of the temperature distribution from the heat diffusion equation in cylindrical coordinate

$$\frac{1}{r}\frac{d}{dr}\Big(r\frac{dT_2(r)}{dr}\Big) - \frac{g}{\kappa_s t}(T_2(r) - T_{amb}) + \frac{q(r)}{\kappa_s} \tag{2.6}$$

where $q(r)$ is the volumetric heating. By solving $T(r)$ and normalize with $q(r)$ and fit with the experimental results he was able to obtained (370 + 650/-320) W/mK for the supported graphene at room temperature. The suspended graphene returns (2500 + 1100/-1050) W/mK at 350 K and decrease to (1400 + 500/-480) W/mK at 500 K. The detailed calculation will be derived in the following chapter.

2.3 Transitional metal dichaclogenides

Transitional metal dichalcogenides (TMDS) are a family of materials with stochiometry of AX_2. TMDs have a wide spectrum of electrical properties from semiconductor-like to metal-like[13]. However, the thermal transport properties have been relatively unexplored because the traditional thermal conductivity measurements such as the 3ω method requires measurable temperature gra-

dient over the thickness[14]. After the techniques and equation developed by Cai et al.[12], researchers have been employing the technique for determining κ of layered materials. In this chapter, two examples from the TMDs family will be given to provide background information and also our attempt to validate the use of opto-thermo techniques on TMDs.

2.3.1 MoS_2

Yan et al.[15] measured the κ of monolayer MoS_2 to be = (34.5 ± 4) W/mK at room temperature. The sample was prepared by mechanical exfoliation and was transferred on to prepatterned $Si_3N_4/SiO_2/Si$ substrate with holes of 1.2 μm in diameter. They observed a saturation behavior for the redshift in power-dependent Raman, which they attributed to nonlinearity terms because the sample was heated to high enough temperature. Both temperature- and power-dependent Raman showed good linear relationship at the temperature ranging from 100 K to 320 K. They also compared the first-order temperature coefficient with different supporting substrate and found out that E^1_{2g} mode is more susceptible to substrate strain than A_{1g} mode[16].

2.3.2 $MoSe_2$

Zhang et al.[17] used similar techniques to determined the κ for mono- and bi-layer MoS_2 and $MoSe_2$. The determined values are (84 ± 17) W/mK and (77 ± 25) W/mK for mono- and bi-layer MoS_2, similar to the results obtained by Yan. The κ for $MoSe_2$ are (59 ± 18) W/mK and (42 ± 13) W/mK for mono- and bi-

layer respectively. In the report, they also determine the interfacial thermal conductance g to be 0.1 to 1 MW/m^{2}K. They determined the g by measuring the temperature increase ΔT with respect to distance from the center of the trench and fit the results with the $T(r)$ determined by (2.6). The outcome g is an order of magnitude lower than previously reported, suggesting that g will affect the extracted κ for trenches with the diameter of 1 μm.

2.3.3 WS_2

Last example in this chapter is WS_2, which has larger bandgap ($\approx$ 2.1eV)[18] than MoS_2. Peimyoo et al.[19] reported 32 W/mK and 53 W/mK for mono- and bi-layer WS_2 using holes of 6 μm in diameter. The calculation details in this paper was not disclosed, but the κ is within the same order of magnitude with MoS_2 and $MoSe_2$.

The above examples show a glimpse of the potential of opto-thermo technique, the technique is suitable for determining κ for layered materials. However, the calculation method will only be valid provide that both the first-order temperature and power coefficient are reasonably linear in the range of interest. Second assumption from (2.6) is that the heat conducts isotropically, therefore the technique will not be accurate for materials with high anisotropicity heat conduction.

CHAPTER 3

HEAT DIFFUSION MODEL

To extract the κ from temperature- and power-dependent Raman spectroscopy, it is essential to first solve the heat dissipation equation for within and outside the suspended region. Temperature distribution within and outside are denoted as $T_1(r)$ and $T_2(r)$ respectively with r is the radial distance from the center of the trench

$$\frac{1}{r}\frac{d}{dr}\Big(r\frac{dT_1(r)}{dr}\Big) + \frac{q(r)}{\kappa} = 0 \; with \; 0 < r \leq R, \tag{3.1}$$

$$\frac{1}{r}\frac{d}{dr}\Big(r\frac{dT_2(r)}{dr}\Big) - \frac{g}{\kappa_s t}(T_2(r) - T_{amb}) + \frac{q(r)}{\kappa_s} = 0 \; with \; r > R \tag{3.2}$$

where $t = 120nm$ is the thickness of the thin film $NbSe_2$ sample, $R = 1.5\mu m$ is the radius of the trench, T_{amb} is the ambient temperature, κ and κ_s are the thermal conductivity of thin film $NbSe_2$ within and outside the suspended region respectively. The difference between (3.1) and (3.2) is the dissipation of heat through thin film $NbSe_2$ to the substrate through g, the interfacial thermal conductance per unit area between thin film $NbSe_2$ and the Si/SiO_2 substrate. Because the thickness is relatively small compare to the dimension of the thin film $NbSe_2$ flake, the heat conducted through the term g will affect the extracted κ when g is less than 20 MW/m^2K. The details will be discussed later in the Parameters section.

The power transfer by the laser beam is normalized by $q(r)$, the volumetric heating (W/m^3) given by

$$q(r) = \frac{I\alpha}{t}\exp\Big(-\frac{r^2}{r_0^2}\Big) \tag{3.3}$$

where $\alpha = (42 \pm 5)\%$ is the absorbance of the thin film $NbSe_2$ at 532nm determined by measurement and $I = P/(\pi r_0^2)$ is the power per unit area at beam

center with r_0 the half Gaussian beam width. (3.2) can be reduced to a nonhomogeneous Bessel's with the use of $\theta = (T_2(r) - T_{amb})$ and $\gamma = \left(\frac{g}{\kappa_s t}\right)^{1/2} r$

$$\frac{\partial^2 \theta}{\partial \gamma^2} + \frac{1}{\gamma}\frac{\partial \theta}{\partial \gamma} - \theta = -\frac{I\alpha}{g}\exp\Big(-\frac{\gamma^2}{\gamma_0^2}\Big) \tag{3.4}$$

The temperature distribution solutions to (3.1) and (3.2) take the form

$$T_1(r) = C_1 + C_2 \ln(r) + C_3 Ei\Big(-\frac{r^2}{r_0^2}\Big) \tag{3.5}$$

$$T_2(r) = C_4 + C_5 I_0(\gamma) + C_6 K_0(\gamma) \tag{3.6}$$

where C_i are coefficient determined by boundary conditions set by the experiment conditions. I_0 and K_0 are the zero-order modified Bessel functions of the first and second kind respectively.

3.1 Boundary conditions and coefficients

There are four boundary equations for determining the coefficients C_i, but some coefficients could be determined with quick analysis. $C_4 = T_{amb}$ and $C_5 = 0$ is obvious by considering $T_2(\infty) = T_{amb}$ because $I_0(\infty) \to \infty$, the first boundary condition stating that the substrate is maintained at room temperature. Since the dimension of the substrate is at least 10^6 times greater than the thin film $NbSe_2$, the temperature increase in the substrate is negligible. The flake is at least 2 times larger than the diameter of the trench in any planar dimension so it gives that the excess heat would be dissipated completely at the edges of the thin film $NbSe_2$. The rest of the coefficient could than be determined by

$$T_2(\infty) = T_{amb} \tag{3.7}$$

$$T_1(r)\mid_{r=R} = T_2(\gamma)\mid_{r=R} \tag{3.8}$$

$$\kappa\frac{dT_1(r)}{r}\mid_{r=R} = \kappa_s\frac{T_2(\gamma)}{r}\mid_{r=R} \tag{3.9}$$

$$-2\pi Rt\kappa_s\frac{T_2(\gamma)}{r}\mid_{r=R} = \alpha P \tag{3.10}$$

We justified (3.7) by stating that the substrate is not heated by the laser and the excess heat on the thin film $NbSe_2$ would dissipate completely at the edge of the flake. (3.8) is the temperature gradient must remained continuous at the trench edge. (3.9) is the energy conservation between the suspended and supported thin film $NbSe_2$, note that the heat could also dissipation through ambient however since the the sample is kept in cryostat pumped to vacuum this path contributes negligibly to the total heat dissipation. (3.10) is another energy conservation related to (3.9), this condition states that the heat flux passing the trench edge must be equal to the heat absorbed by the thin film $NbSe_2$. With the above boundary equations we can solve the remaining coefficient.

With $T_1(0)$ must be finite, we can obtain $C_2 = -2C_3$ by taking derivative of both sides of (3.5).

$$0 = C_2\frac{\partial \ln(r)}{\partial r} + C_3\frac{d\partial Ei(-\frac{r^2}{r_0^2})}{\partial r} = \frac{C_2}{r} + \frac{C_3 exp(-\frac{r^2}{r_0^2})}{-\frac{r^2}{r_0^2}} \times \frac{-2r}{r_0^2} \tag{3.11}$$

The last coefficient left in (3.2) can be determined by (3.10)

$$C_6 = \frac{\alpha P}{2\pi Rt\kappa_s\gamma K_1(R\gamma)} \tag{3.12}$$

With $T_2(r)$ solved, we can move on to solve the coefficients in $T_1(r)$. By (3.9)

$$C_3 = \frac{\alpha P}{2\pi Rt\kappa_s\gamma K_1(R\gamma)}\frac{\kappa_s\gamma K_1(R\gamma)}{\frac{2\kappa}{2}\Big[exp\Big(-\frac{R^2}{r_0^2}\Big)-1\Big]} \tag{3.13}$$

Note that the derivative of $K_0(\gamma)$ is

$$\frac{\partial K_0(\gamma)}{\partial r} = K_1(\gamma)\Big(\frac{g}{\kappa_s t}\Big)^{1/2} \tag{3.14}$$

With only C_1 and (3.7) left, we solve the constant term for (3.5)

$$C_1 = T_{amb} + \frac{\alpha P}{2\pi R t \kappa_s \gamma K_1(R\gamma)} \frac{\kappa_s \gamma K_1(R\gamma)}{\frac{2\kappa}{2}\left[exp\left(-\frac{R^2}{r_0^2}\right) - 1\right]} \times \left[E_i(-\frac{R^2}{r_0^2}) - 2\ln(R)\right] - \frac{K_0(R\gamma) \times \alpha P}{2\pi R t \kappa_s \gamma K_1(R\gamma)} \tag{3.15}$$

The entire solution $T_1(r)$ takes the form

$$T_1(r) = T_{amb} + \frac{\alpha P}{2\pi R t \kappa_s \gamma K_1(R\gamma)} \frac{\kappa_s \gamma K_1(R\gamma)}{\frac{2\kappa}{2}\left[exp\left(-\frac{R^2}{r_0^2}\right) - 1\right]} \times \left[E_i(-\frac{R^2}{r_0^2}) - 2\ln(R)\right]$$

$$- \frac{K_0(R\gamma) \times \alpha P}{2\pi R t \kappa_s \gamma K_1(R\gamma)} + \frac{\alpha P}{2\pi R t \kappa_s \gamma K_1(R\gamma)} \frac{\kappa_s \gamma K_1(R\gamma)}{\frac{2\kappa}{2}\left[exp\left(-\frac{R^2}{r_0^2}\right) - 1\right]} \times \left[E_i(-\frac{r^2}{r_0^2}) - 2\ln(r)\right] \tag{3.16}$$

Below shows a calculated temperature profile $T(r)$ for different values of κ, the higher the κ the lower the temperature increase. In general, the temperature distribution $T(r)$ for higher κ is relatively independent of g. The manifestation of g can be seen at temperature distribution outside the trench $T_2(r)$. Essentially all the heat needs to be dissipated by g at the edge of the thin film $NbSe_2$, the '*pinning*' effect of g will be discussed in detail later.

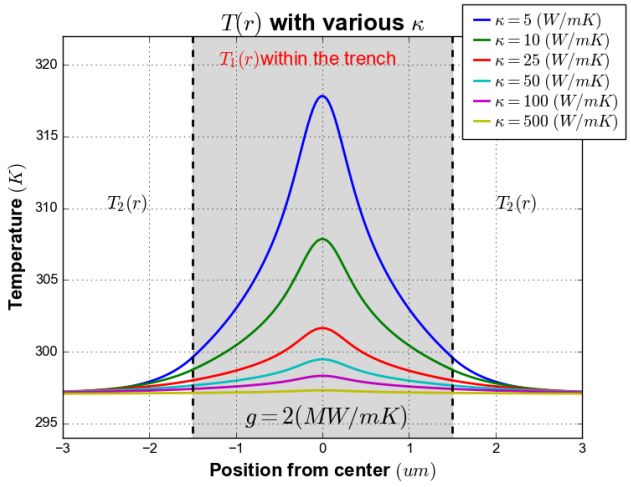

Figure 3.1: Example stacking of $T(r)$ for different κ.

An example stacking of $T_1(r)$ and $q(r)$ is show in Figure 3.2. Note that because of low interfacial thermal conductance ($g = 2$ MW/m^{2}K), temperature

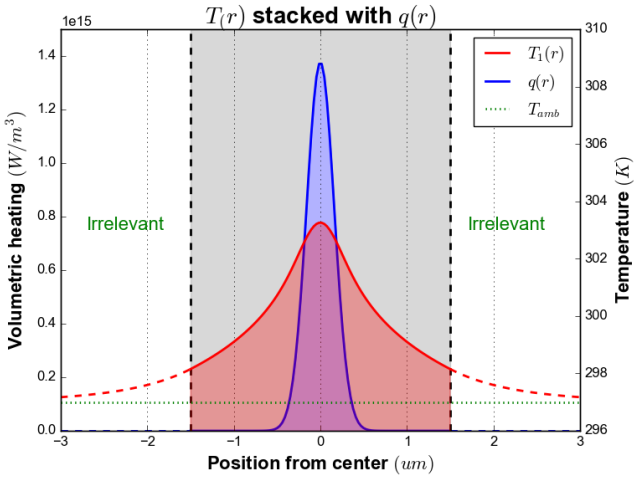

Figure 3.2: Example stacking of $T(r)$ and $q(r)$ plot.

increases (Difference between $T(r)$ adn T_{amb}) even outside the trench. The distribution needs to be normalized to reflect the collective response we obtained from Raman measurements, so we further normalized by the *angle* to obtain the averaged weighted T_m

$$T_m \approx \frac{\int_0^\infty T(r) r \exp\left(-\frac{r^2}{r_0^2}\right) dr}{\int_0^\infty r \exp\left(-\frac{r^2}{r_0^2}\right) dr} \tag{3.17}$$

The nominator and the denominator of (3.17) can be seen in Figure 3.3. The nominator is the area under red curve and the denominator is the area under the blue curve, also note that the Gaussian beam width is much smaller than the trench diameter therefore the heating outside the trench due to laser is negligible. The reason why T_m contains $T(r)$ rather than $T_1(r)$ is because we have to consider the entire temperature distribution due to laser heating, however the model will be inaccurate if region outside the trench is also heated by laser outside the trench. If the Guassian beam width is larger than the trench, then we have to consider both the interfacial conductance g and supported thermal conductivity κ_s as they will change the temperature distribution $T(r)$ significantly

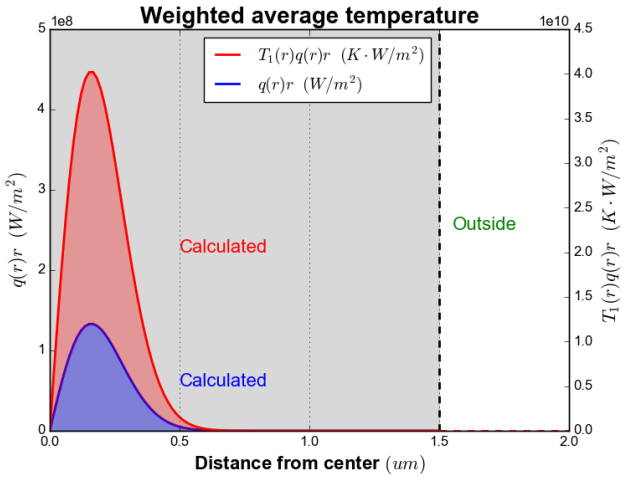

Figure 3.3: Visualization of T_m calculation.

since (3.10) will not hold true for this case. Therefore, it is essential for the Gaussian beam width to be less than the diameter of the trench. We can simplify the equation by replacing $T(r)$ by $T_1(r)$ if the diameter is much larger than Gaussian beam width without much deviation as $T_1(r)q(r)r$ decays quickly outside the Gaussian beam width (The red curve is roughly same width as the blue curve).

Finally we determined the thermal conductivity κ by fitting (3.17) to the experimental result (T_{exp})

$$T_{exp} = T_{amb} + \frac{\chi_P}{\chi_T} P \tag{3.18}$$

3.2 Parameters

In this section simulations for each individual parameter is presented in hope to provide readers an fundamental understanding of the errors accompanied with the parameter. All simulations use the first-order temperature coefficient from sample 161027_HL_NbSe2 and first-order power coefficient from sample

161027_HL_NbSe2. The initial parameters are Half Gaussian beam width r_0 = 0.22 μm, Absorption coefficient α = 0.42 determined by measurement which will later be discussed in *Measurement setup*, interfacial thermal conductivity g = 2 MW/m^{2}K , and lastly the supported thermal conductivity $\kappa_s = \kappa$. Each subsection varies only the specify parameter while the others remained fixed to enable us to see the general trend regarding the specify parameter.

3.2.1 Half Guassian beam width r_0

As mentioned in the previous section, it is essential that the Guassian beam width to be smaller the trench diameter so the supported thin film $NbSe_2$ will not be heated by the laser as (3.10) will be invalid if that is not the case. The half Guassian beam width is estimated to be 0.26μm, 0.23 μm, and 0.19μm for long-working distance 50×, 50×, and 100× with $r_0 = \lambda/\pi$NA[12]. The simulated 3D drawing of $q(r)$ is shown on next page. In Figure. (3.7), the peak $q(r)$ for 100× is almost twice of the peak $q(r)$ for long-working distance 50×. However, since the Gaussian width is sufficiently smaller than the diameter of the trench, all lens should obtain similar κ. In fact, in the experimental section we do obtained similar results even with different lenses (see Appendix A).

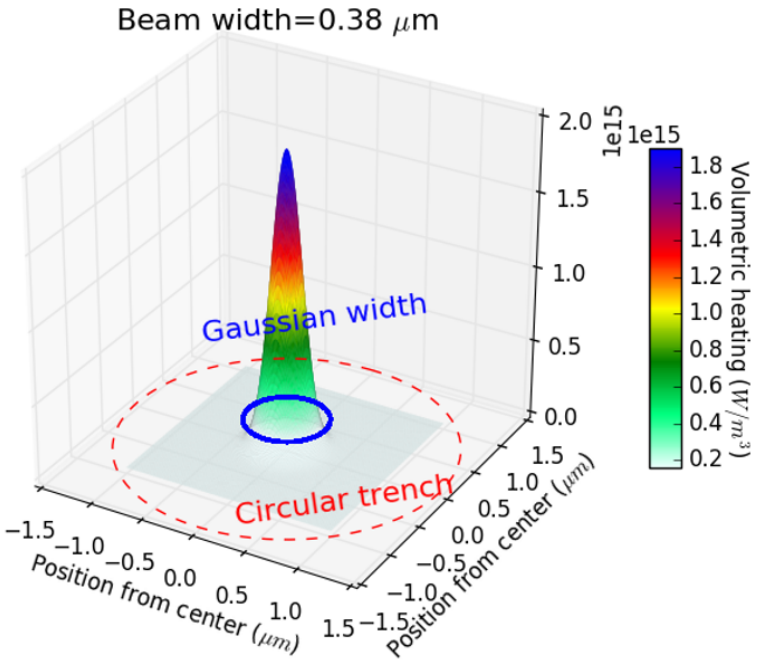

Figure 3.4: $q(r)$ for 100X NA=0.9 lens

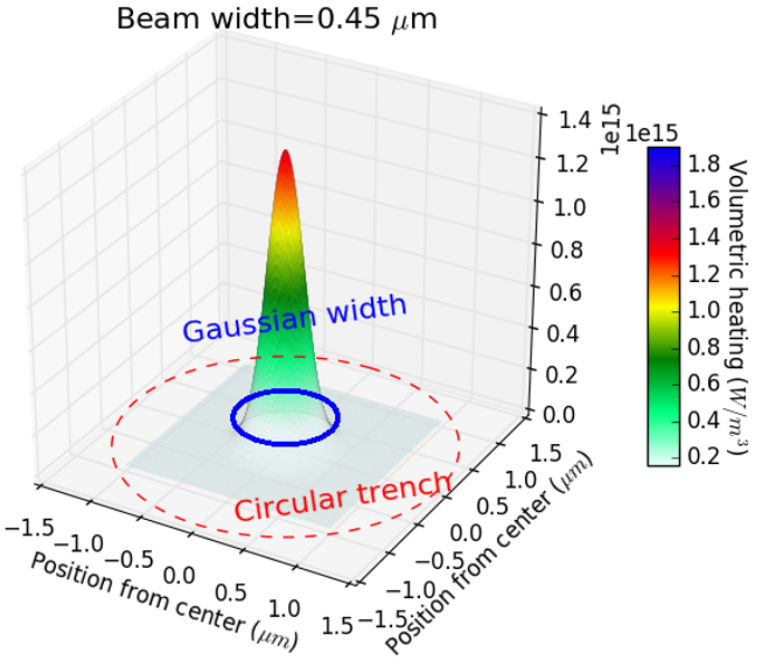

Figure 3.5: $q(r)$ for 50X NA=0.75 lens.

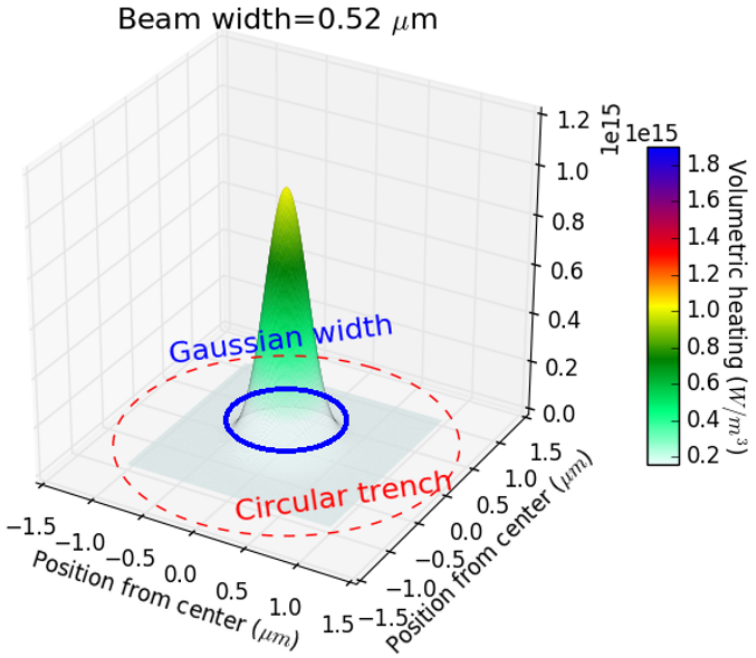

Figure 3.6: $q(r)$ for long-working distance 50X NA=0.65 lens.

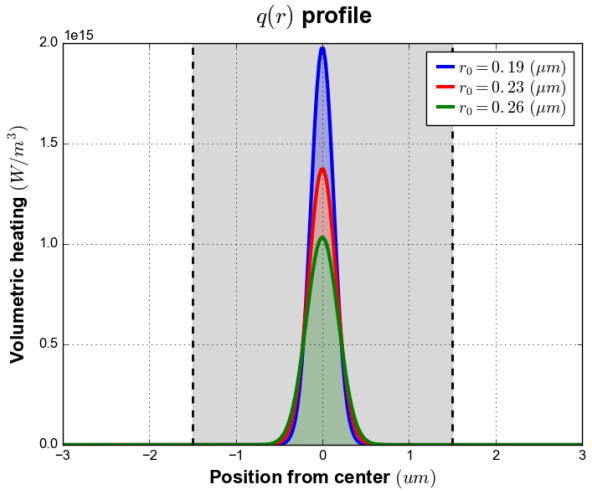

Figure 3.7: $q(r)$ stacking for 100X, 50X, and LW 50X lens.

Lastly in this subsection let's consider the variation resulting from r_0 by fixing all the other parameters, including the first-order temperature and power coefficients. In the experiments, however, the first-order temperature and power coefficients will be different for different r_0.

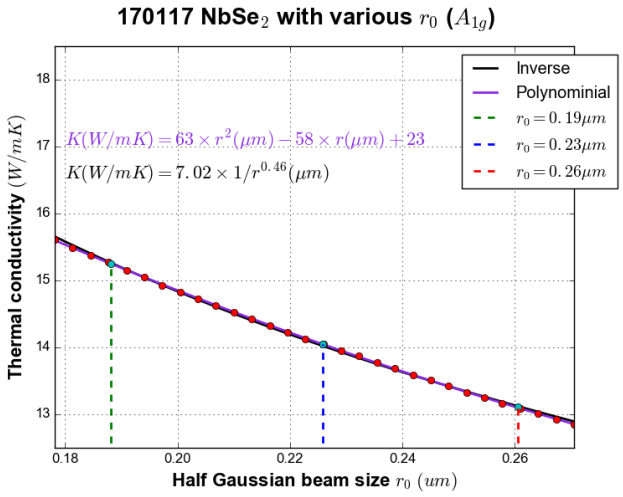

Figure 3.8: κ for various r_0 using A_{1g}.

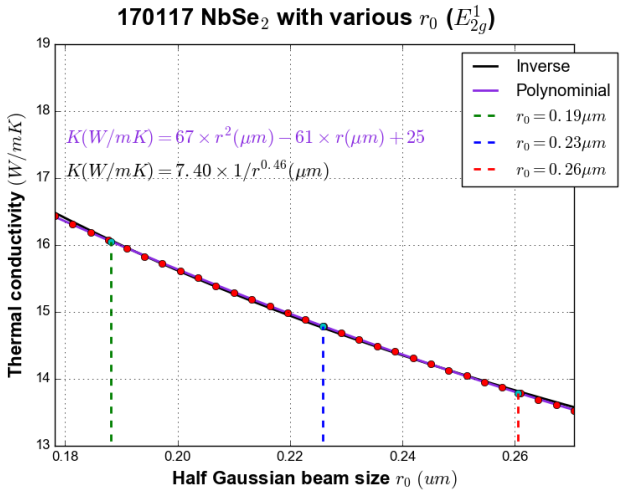

Figure 3.9: κ for various r_0 using E^1_{2g}.

Both the *Inverse* and the second-order *Polynomial* fittings could describe the relation between r_0 and κ reasonably well. The actual lens used for 161027_*HL_NbSe*2 is the 50× NA= 0.75, so the extracted κ is (14.4 ± 4) W/mK depending on which Raman mode we use. The importance in this plot is that the error of r_0 could result in different κ rather than the exact value itself. In the later *Experimental* chapter, we will take this uncertainty into account.

3.2.2 Absorption coefficient α

Absorption coefficient α is the portion of the power absorbed by thin film $NbSe_2$. α's role in determining the temperature distribution $T(r)$ lies in (3.10), the total power conservation equation. Since α does not affect the *shape* of the temperature distribution $T(r)$, the extracted κ varies linearly with α.

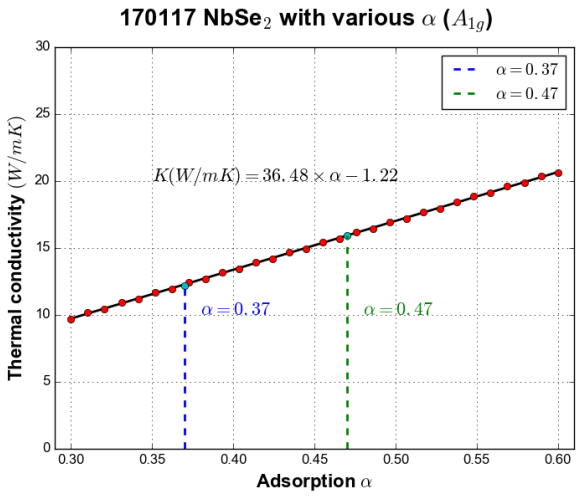

Figure 3.10: κ for various α using A_{1g}.

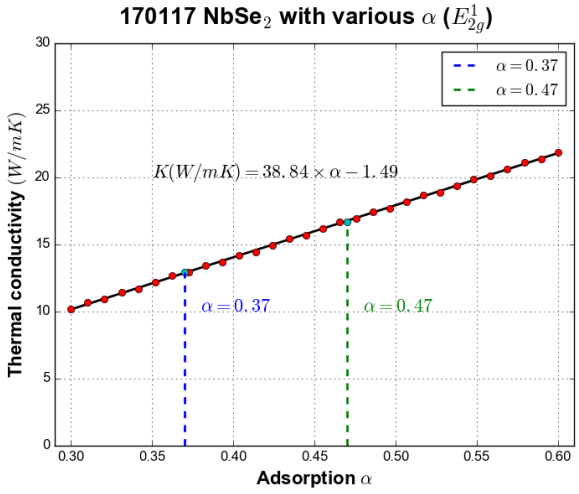

Figure 3.11: κ for various α using E^1_{2g}.

3.2.3 Interfacial thermal conductance g

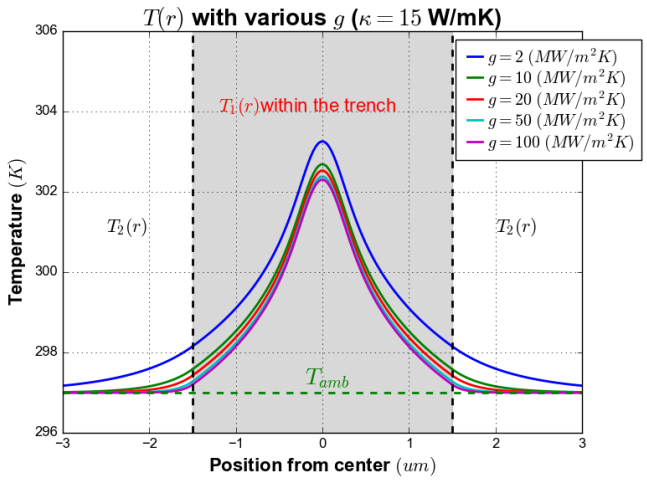

Figure 3.12: $T(r)$ for various g using κ = 15 W/mK.

The interfacial thermal conductance g plays a big role in determining the temperature distribution $T(r)$. Figure 3.12 shows an example for various temperature distribution $T(r)$ corresponding to different g. The affect for various g can be seen at the absolute temperature at the edge. The '*pinning*' to ambient temperature is more prominent for higher g. As seen in Figure 3.12, the temperature distribution $T(r)$ does not change significantly after g = 20 MW/m^{2}K. After this saturation of heat dissipation through substrate, the extracted κ becomes relatively independent of g. The interfacial thermal conductance is assumed to be g = 2 MW/m^{2}K for κ extraction, which is the experimental value range for graphene[6], MoS_2[6][20], and $MoSe_2$[20] on SiO_2.

Figure 3.13 and Figure 3.14 both show similar trend which could be described by inverse fitting equation. The extracted thermal conductivity κ for A_{1g} mode is roughly 0.5 W/mK lower than E^1_{2g} mode for same interfacial thermal conductance g.

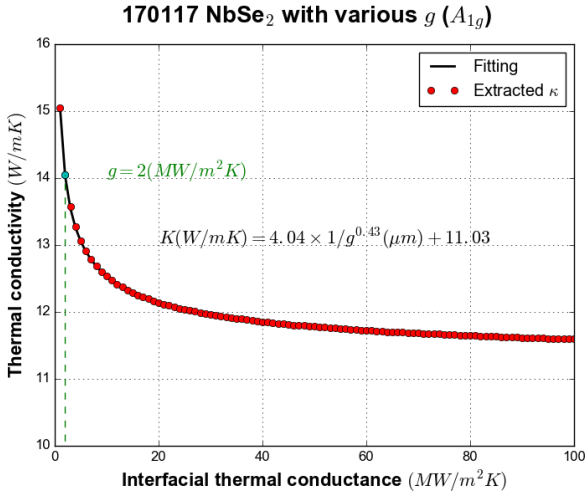

Figure 3.13: Extracted κ for various g, A_{1g} mode.

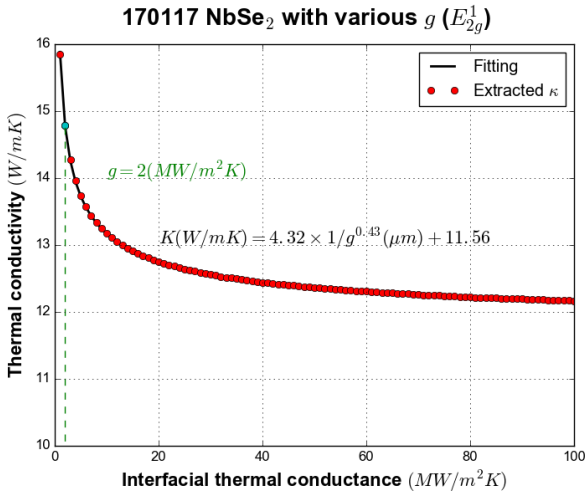

Figure 3.14: Extracted κ for various g, E^1_{2g} mode.

3.2.4 Supported thermal conductivity κ_s

The effect of supported thermal conductivity of thin film $NbSe_2$ κ_s on the temperature distribution $T(r)$ is similar to g. However, rather than pinning the temperature at the edge of the trench to T_{amb}, higher κ_s to κ ratio conducts more heat to the edge of the thin film $NbSe_2$ edge. If we extrapolate $\kappa_s = 0$ W/mK, the

extracted κ will be similar to the case of which g is extrapolate to infinity; if we set $\kappa_s = \kappa$, the extracted κ will be determined by g alone. In both cases which either $\kappa_s = 0$ W/mK or $g \to \infty$ MW/m^{2}K, the extracted κ is closed to 12 W/mK.

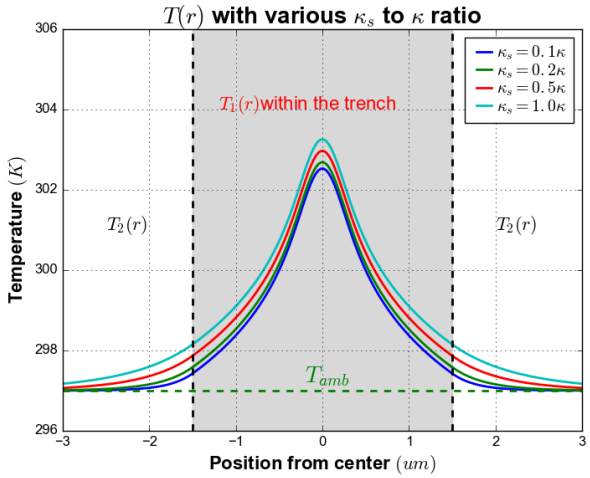

Figure 3.15: $T(r)$ for various κ_s to κ ratio.

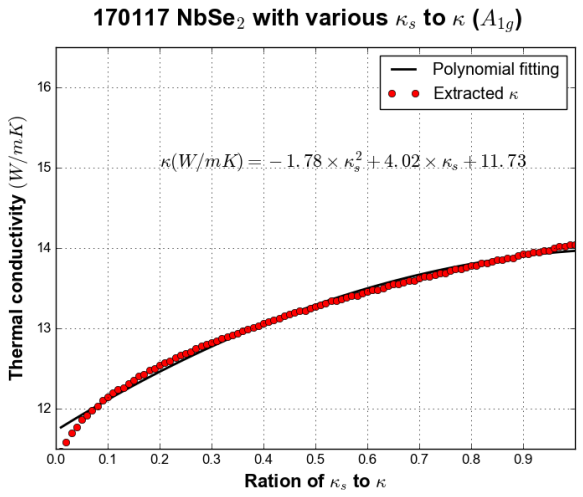

Figure 3.16: Extracted κ for various κ_s to κ ratio, A_{1g} mode.

In Figure 3.15, the temperature distribution $T(r)$ is similar to Figur 3.12. The '*pinning*' effect is more prominent at lower supported thermal conductivity κ_s, which the temperature increase is restricted within the trench and the heat is

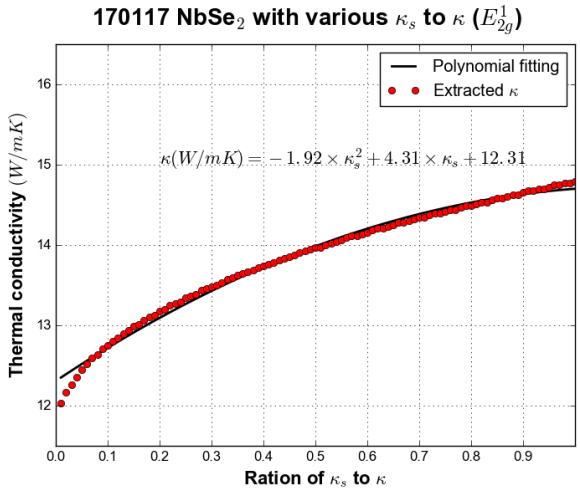

Figure 3.17: Extracted κ for various κ_s to κ ratio, E^1_{2g} mode.

conducted through substrate at the trench edge. Figure 3.16 and Figure 3.17 show the dependence of κ to κ_s, again the extracted thermal conductivity κ for A_{1g} mode is roughly 0.5 W/mK lower than E^1_{2g} mode for same κ_s to κ ratio. However since the thin film $NbSe_2$ and the substrate are bounded only by van der Waals force, κ_s is assumed to be same as κ for final extraction.

To conclude, for the parameters analyzed in this chapter, the extracted κ will have the maximum difference of 4 W/mK. The uncertainty of absorption coefficient α will be the dominant factor of this difference since κ varies linearly with α. Difference from both g and κ_s will only be large in the extreme cases therefore are assumed to be minor factor of the κ difference.

CHAPTER 4

TEMPERATURE- AND POWER-DEPENDENT RAMAN

In this chapter, detailed descriptions for the measurements and the results will be discussed. The main focus of this chapter is to provide readers a experimental guide to the opto-thermo technique, which can be employed on other 2-D materials of interest in the future. The data mentioned in this chapter is the final data used for κ extraction.

4.1 Sample preparation

The $NbSe_2$ sample was prepared by mechanically exfoliating commercially available bulk $NbSe_2$ crystal (HQ graphene Inc.) and transferred to prepatterned Si/SiO_2 substrates within 90 min to minimize oxidation. The trenches was etched down from the $Si0_2$, ranging from 100 – 200nm in depth to prevent contact between the thin film $NbSe_2$ and the substrate due to deflection. There are two substrates used in the experiments, one for temperature-dependent Raman and the other for power-dependent Raman. The temperature-dependent Raman was done on linear trench shown in Figure 4.2 and 4.3. The advantages of linear trench include easier sample preparation and relatively resistive to lateral shaking. However for power measurements, circular trench is preferred because the inadequate modeling for linear flakes. The power-dependent measurement was done on circular trench shown in Figure 4.4 and 4.5. The optical image of $161027\_HL\_NbSe_2$ and $170117\_HL\_NbSe_2$ is shown in Figure 4.1, both are taken using 100×.

Figure 4.1: Optical image of 161027_*HL_NbSe*$_2$ and 170117_*HL_NbSe*$_2$.

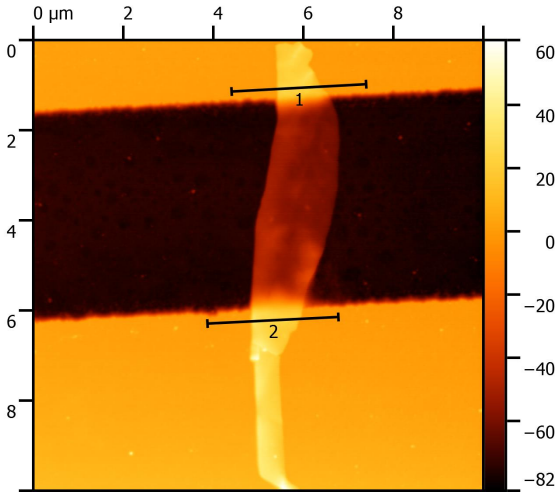

Figure 4.2: AFM image of 161027_*HL_NbSe*$_2$ for temperature-dependent Raman.

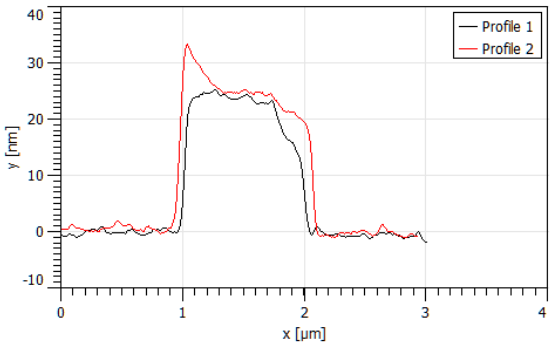

Figure 4.3: Step height of 161027_*HL_NbSe*$_2$, the sample is measured to be 25 nm.

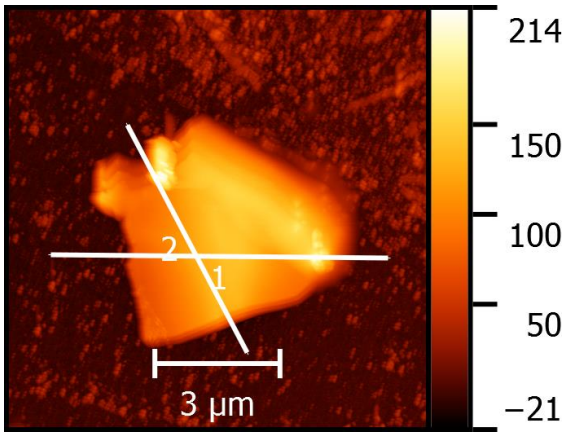

Figure 4.4: AFM image of 170117_*HL_NbS e*$_2$ for power-dependent Raman.

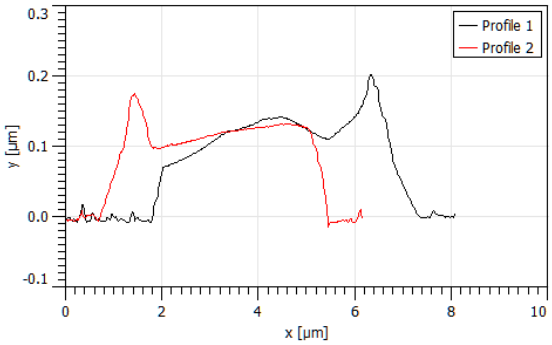

Figure 4.5: Step height of 170117_*HL_NbS e*$_2$, the sample is measured to be 120 nm.

4.1.1 Surface roughness and flake thickness

The NbSe2 sample on the circular trench is much thicker that the sample on the linear trench. It is believed that the transferring of the flake would be easier if transferring from a rougher material to a smoother substrate because the interaction between flake and the material is most likely to be van der Waals force[1]. Therefore it is more difficult to transfer a thinner flake onto a rough substrate and vice versa.

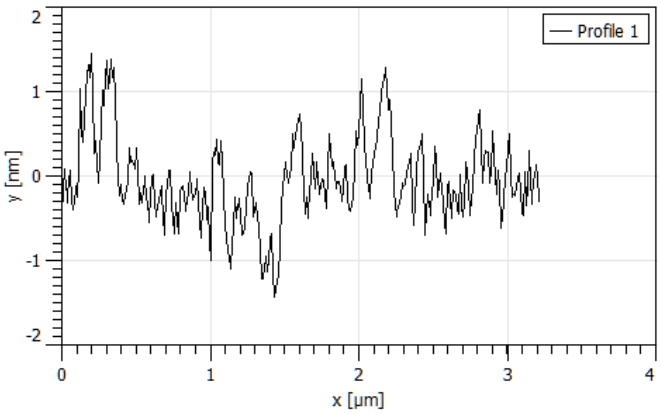

Figure 4.6: The RMS for the linear trench is measured to be 0.9 nm.

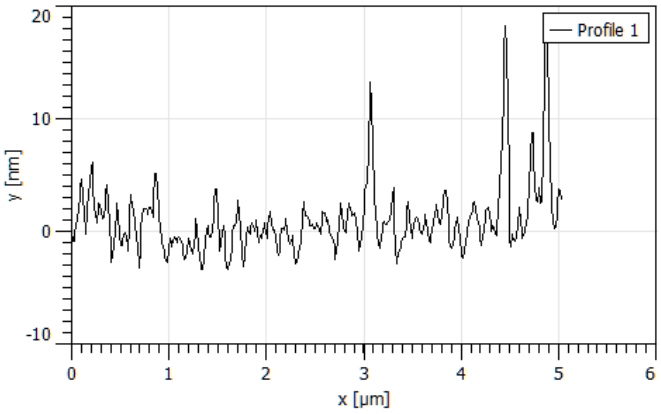

Figure 4.7: The RMS for the circular trench is measured to be 4.16 nm.

4.2 Measurement setup

In this section, descriptions of the apparatus and the procedure will be provided. The three system will be discussed here includes: Renishaw InVia Confocal Raman microscope system, Oxford Instrument cryostat, and absorption coefficient measurement.

4.2.1 Raman system

Raman spectra were obtained using Renishaw InVia Confocal Raman microscope system with 532nm laser excitation. The temperature-dependent spectra was collected using long-working distance 50× objective with 0.65 NA. The laser power for temperature-dependent Raman was maintained below 0.1 mW to avoid excess heating of the sample. Power-dependent Raman spectra was obtained using 50× and 100× with NA of 0.75 and 0.9 respectively. The half Guassian beam width is estimated to be 0.26μm, 0.22 μm, and 0.19μm for long-working distance 50×, 50×, and 100× with $r_0 = \lambda/\pi$NA[12]. The grating was 2400 l/mm for all measurements and the spectral resolution was ~1.1 cm^{-1}. All measurements were calibrated using silicon peak at 520.6 cm^{-1} before any data was collected.

4.2.2 Cryostat

The thin film $NbSe_2$ sample was kept in cryostat (Oxford Instrument) with controllable heating stage, the temperature error was kept within ± 1K by stabilizing the temperature for 10 min. The reason that we didn't use the cryostat for power-dependent measurement is that the window of the cryostat broadens the laser beam, therefore less power is deposited onto the thin film $NbSe_2$. The cryostat also have another inherit problem which is the shaking caused by the pumps. There are two pumps for the cryostat system, one is the turbo pump to pump the cryostat and another is the mechanical pump to deliver the liquid nitrogen from the dewar. Even with isolations the shaking cannot be reduced to less than 1 μm, this will change the half Guassian beam width r_0 significantly

thus making the power-dependent Raman measurements less reliable.

4.2.3 Absorption coefficient

The absorption coefficient of the thin film $NbSe_2$ is determined by the setup schematic shown in Figure 4.8.

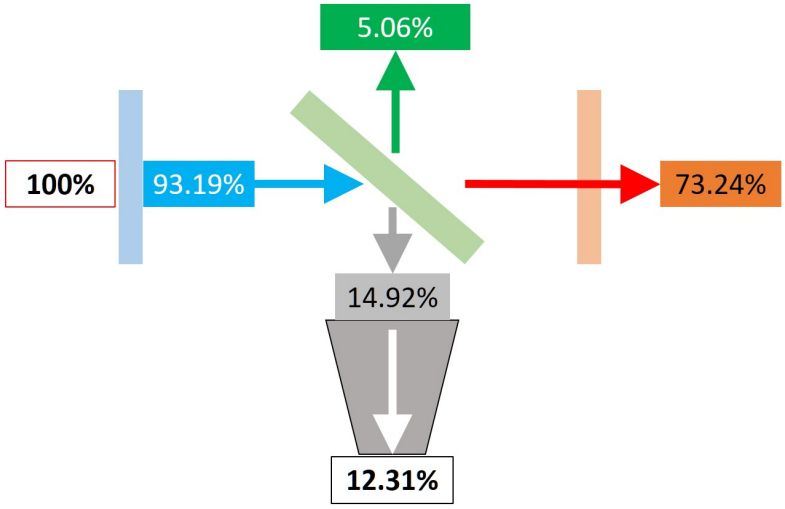

Figure 4.8: Schematic drawing of absorption measurement, the value in the box indicate the percentage measured at the terminal. The value measured before the light blue lens (red box) is set as the initial value.

The calculated transmission of each component is shown in Figure 4.9. The arrow represents the transmission path of the component calculated. Note that most of the power is lost through the beam splitter. We can then use the calculated percentage to determine the actual power incident and reflected on the sample, which is placed under the lens drawn in gray.

Now we can calculate the actual power reflected by the Si/SiO_2, which is done by dividing the final value (green box) by the transmission percentages of

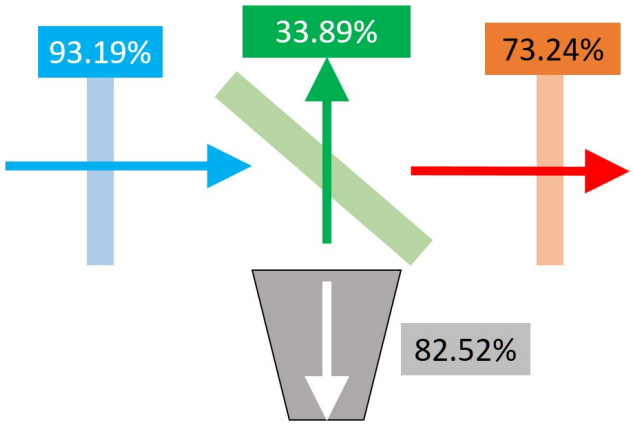

Figure 4.9: The transmission percentage of each individual component. The transmission of the beam splitter (light green) and the lens (gray) are used.

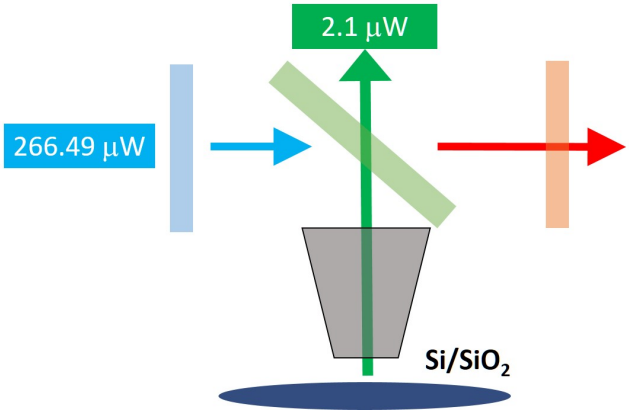

Figure 4.10: The calibration measurement using Si with 200 μm SiO_2, the values in the boxes are absolute values measured.

the components along the beam path (green arrow).

$$R_{Si/SiO_2} = 2.1 \times \frac{1}{33.89\%} \times \frac{1}{82.52\%} = 7.51\ \mu W \tag{4.1}$$

The first fraction is the power lost through the beam splitter and the second is the power lost through the lens. The reflectance is calculated to be 7.51/32.817 = 22.88 % where 32.817 μ W is the power incident on the Si/SiO_2 by 266.49 $\times$

12.31%. The reflectance is within 20 35 %,which is similar for literature data bare silicon and silicon after a prolong exposure[21].

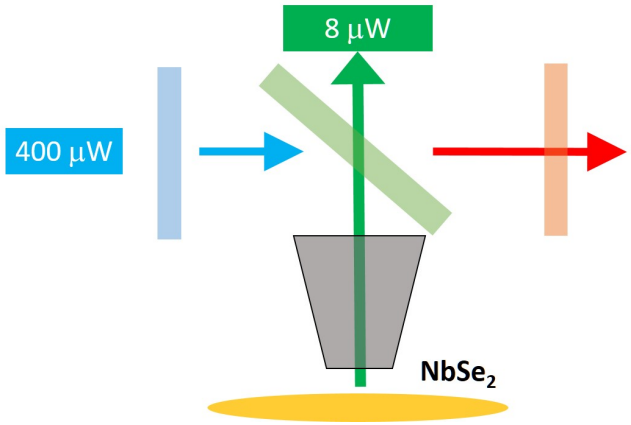

Figure 4.11: The absorption measurement data of 100nm $NbSe_2$ sample.

The measurement data for 100nm $NbSe_2$ sample is shown schematically in Figure 4.11. With similar calculation, the actual power reflected by the 100 nm $NbSe_2$ sample is

$$R_{NbSe2_2} = 8 \times \frac{1}{33.89\%} \times \frac{1}{82.52\%} = 28.61\ \mu W \tag{4.2}$$

Finally the reflectance is calculated to be 28.61/49.24 = 58.1 % where 49.24 μW is the power incident on the Si/SiO_2 by 400 × 12.31%. Since the flake is opaque so we assumed the absorption coefficient to be 100 – 58.1 ~ 42%.

4.3 Results

To quantify the effect of temperature and power on Raman spectra, both A_{1g} and E^1_{2g} modes were fitted using Lorentzian fit as shown in Figure 4.12. The

center of the fitting is used throughout the calculations and the FWHM of the fitting for temperature-dependent Raman spectra is recorded. Two peaks are used here: A_{1g} mode at 230.9 cm^{-1} and E^1_{2g} mode at 238.3 cm^{-1}[22]. The Raman shift for both peaks are within 10 cm^{-1}, therefore it is hard to distinguish the peaks at both low and moderate power. The reason for low power is that A_{1g} mode will be very dominant and thus making it difficult to differentiate the E^1_{2g} mode. At moderate power it is because the first-order power coefficient for E^1_{2g} mode is two times larger than A_{1g} mode, so at moderate power two modes merge together. However at high enough power the Raman shift will saturates and the modes become distinguishable again.

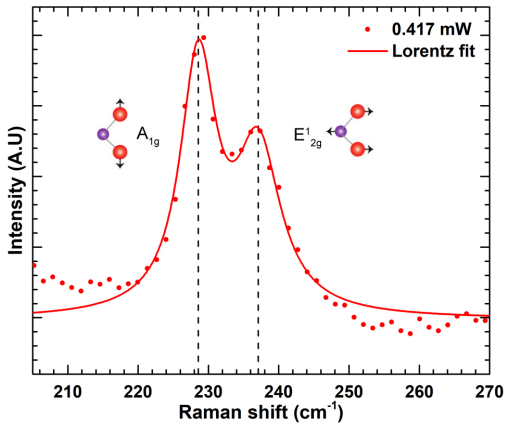

Figure 4.12: Example Lorentzian fitting.

4.3.1 Temperature-dependent Raman

The peaks showed redshift with increasing temperature and power, and the thermal effect can be described by Grüneisen model[23]

$$\omega(T) = \omega_{T_0} + \chi_T T \tag{4.3}$$

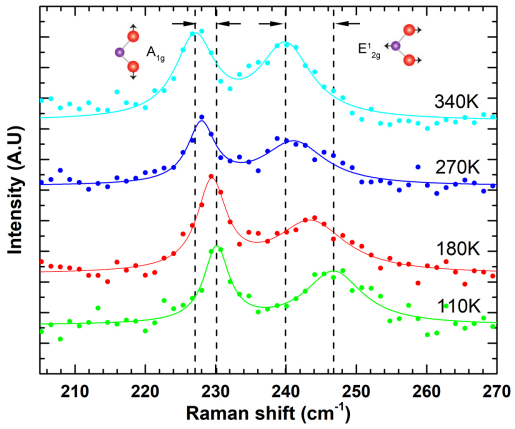

Figure 4.13: Example Lorentzian fitting for 110 K, 180 K, 270 K, and 340 K.

where ω_{T_0} is the intercept of Raman shift when flake temperature T approach 0 K. χ_T is the first-order temperature coefficient for A_{1g} and E^1_{2g} modes which can be derived from the slope of temperature dependence. The Raman frequency shift due to temperature can be described by thermal expansion and other anharmonic effect which can be observed in silicon[7] and other layered selenide systems[24]. Nonlinearity from higher-order terms can been seen on other TMDs materials[25] and are expected to be more dominant at higher temperature[10], however linear dependence is desired for extracting κ at temperature range of interest.

Figure 4.13 shows temperature-dependent data for both 20 nm and 25 nm flakes with Lorentzian peak position fit for A_{1g} and E^1_{2g} modes plotted as functions of temperature.The temperature coefficients for A_{1g} mode are $-(0.0157 \pm 0.0005)$ cm^{-1}/K and $-(0.0148 \pm 0.0006)$ cm^{-1}/K for 20 nm and 25 nm respectively. E^1_{2g} mode peaks have twice the redshift compare to A_{1g} mode and their temperature coefficients are $-(0.0379 \pm 0.0019)$ cm^{-1}/K and $-(0.0341 \pm 0.0021)$ cm^{-1}/K for 20 nm and 25 nm respectively. The slope is more negative for 20 nm

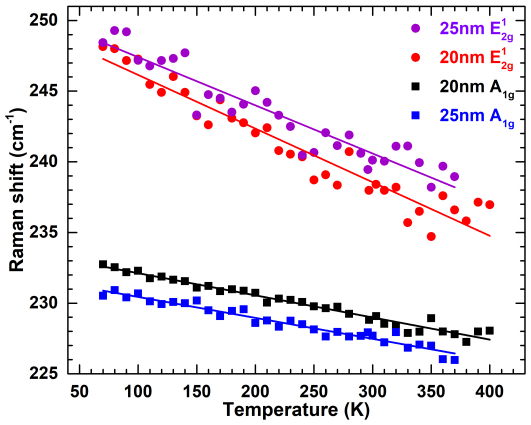

Figure 4.14: Raman shift of 25 nm and 20nm $NbSe_2$ with respect to temperature using linear trench.

flake because the temperature range is larger, which higher-order terms contribute to nonlinearity. The larger fitting error for E^1_{2g} mode can be attributed to the broad nature of the peak shape as in Figure 4.13 which have lower signal-to-noise ratio, however, FWHM (Figure 4.15) for E^1_{2g} mode does not increase with temperature while A_{1g} mode does; A_{1g} mode on the other hand, have small fitting error because of higher signal-to-noise ratio.

Table 4.1 shows the experimental data for temperature-dependent Raman spectra. The first-order temperature coefficients χ_T for both 25 nm and 20 nm flakes are similar, suggesting that the first-order temperature coefficient chi_T is relatively independent of thickness for thin film $NbSe_2$. The values of 25 nm sample ($161027\_HL\_NbSe_2$) are used for κ extraction because the thickness is closer to the sample in power-dependent Raman spectra ($161027\_HL\_NbSe_2$). AFM image and section height of 20 nm sample ($161020\_HL\_NbSe_2$) are shown in Figure A.8 and Figure A.9.

Table 4.1: First-order temperature coefficient

Thickness	Raman mode	T range (K)	χ_T (cm^{-1}/K)	ω_{T_0} (cm^{-1})
25 nm	E^1_{2g}	70~370	−0.03408 ± 0.0021	250.815
25 nm	A_{1g}	70~370	−0.01482 ± 0.0006	231.925
20 nm	E^1_{2g}	70~400	−0.03794 ± 0.0019	249.942
20 nm	A_{1g}	70~400	−0.01566 ± 0.0005	233.689

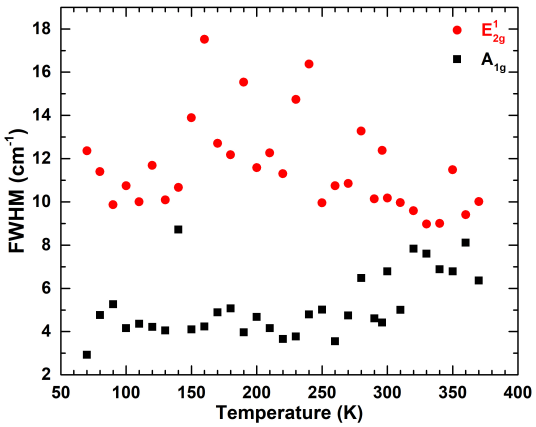

Figure 4.15: FWHM for 161027_*HL_NbSe*2 with respect to temperature, the FWHM of A_{1g} mode increases after 250K while no trend observed for E^1_{2g} mode.

The FWHM at each temperature is plotted in Figure 4.14. Linear dependence for A_{1g} mode is observed starting from 250 K. No similar dependence is observed for E^1_{2g}. The FWHM for both modes are within reasonable range to be used in κ extraction.

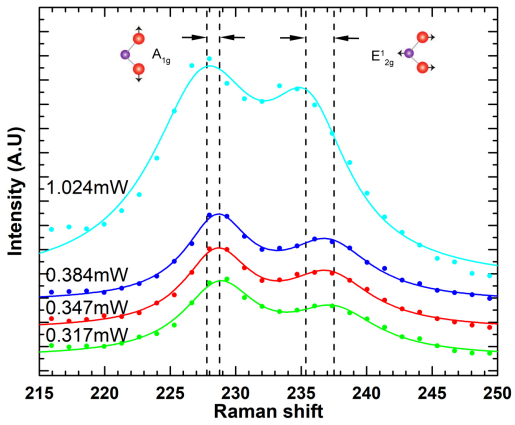

Figure 4.16: Example Lorentzian fitting for 0.317 mW, 0.347 mW, 0.384 mW, and 1.024 mW.

4.3.2 Power-dependent Raman

Likewise we can fit the first-order power coefficient at low power described by

$$\omega(P) = \omega_{P_0} + \chi_P P \tag{4.4}$$

where P is the laser power and ω_{P_0} is the intercept of Raman shift when P approach 0. Both Raman modes exhibit good linearity dependence between 0.3 mW and 1.7 mW, above that the Raman shift saturates as seen in Figure 4.17. The saturation could be the consequence of nonlinearity higher-order terms from higher temperature. The first-order coefficients are $-(2.987 \pm 0.091)$ cm^{-1}/mW and $-(1.359 \pm 0.091)$ cm^{-1}/mW for A_{1g} and E^1_{2g} modes respectively. The E^1_{2g} mode shifted more than twice of A_{1g} mode, which showed higher dependence of laser power.

The sensitive responses to both temperature and power indicates strong localized heating affect, which we can probe the local temperature by the measured the Raman frequency change. By combining the two data and fitted using

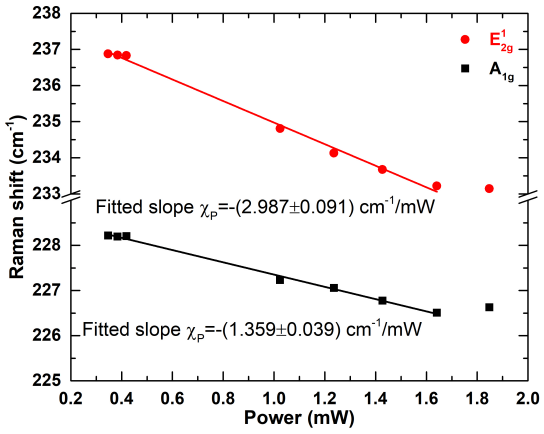

Figure 4.17: Raman shift of 120nm $NbSe_2$ with respect to power using circular trench.

Table 4.2: First-order power coefficient

Thickness	Raman mode	P range (mW)	χ_P (cm^{-1}/mW)	ω_{P_0} (cm^{-1})
120 nm	E^1_{2g}	0.347~1.641	-2.987 ± 0.091	237.962
120 nm	A_{1g}	0.347~1.641	-1.359 ± 0.039	228.713

(3.17), the extracted κ is shown in Table. 4.3

Table 4.3: Extracted κ using different χ_T and χ_P

Raman mode	χ_P (cm^{-1}/mW)	χ_T (cm^{-1}/K)	κ (W/mK)
E^1_{2g}	-2.987 ± 0.091	-0.03794 ± 0.0019	14.78
A_{1g}	-1.359 ± 0.039	-0.01566 ± 0.0005	14.05
E^1_{2g}	-2.987 ± 0.091	-0.03408 ± 0.0021	16.62
A_{1g}	-1.359 ± 0.039	-0.01482 ± 0.0006	14.94

The χ_P are from $170117\_HL\_NbSe_2$ (120nm) and the χ_T in the first two columns are from $161027\_HL\_NbSe_2$ (25nm) and the latter two are from

161020_HL_NbSe$_2$ (20nm). The extracted κ does not vary significantly with the χ_T of different thickness. Another consideration is the penetration depth of Niobium Diselenide, which is estimated to be 30 nm [26] and the absorption coefficient is 0.3 for 30nm flakes[27]. With that the extracted thermal conductivity κ then becomes (39 ± 0.5) W/mK. However, this is under the assumption that χ_P does not change with thickness. Decrease in the absolute value of χ_P was observed in both MoS_2 and $MoSe_2$ from monolayer to bilayer[20] by a least 25%. χ_P is very sensitive to thickness and therefore has to be experimentally verified to draw further conclusions.

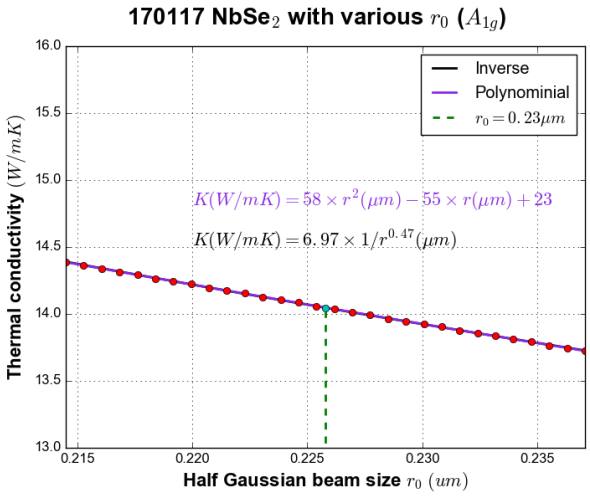

Figure 4.18: κ difference resulting from Gaussian beam width deviation using A_{1g} mode.

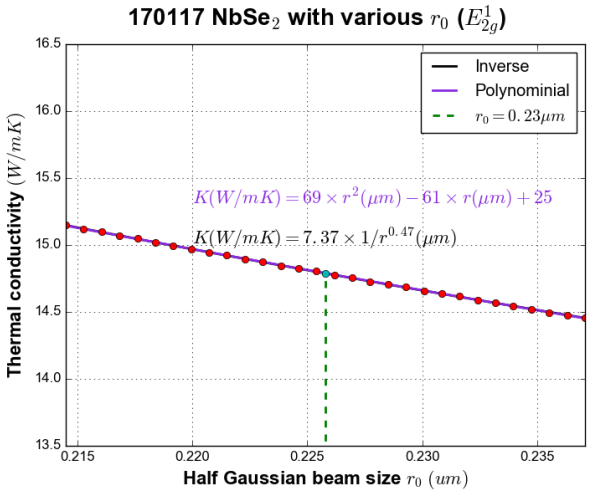

Figure 4.19: κ difference resulting from Gaussian beam width deviation using E^1_{2g} mode.

CHAPTER 5

HALL MEASUREMENT

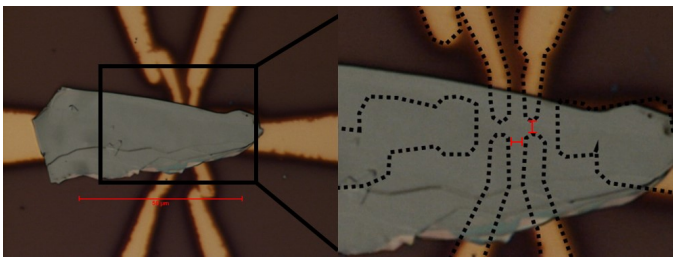

Figure 5.1: From the left, 100× optical image of $NbSe_2$ on prepatterned Hall bar substrate. Dotted lines show the Hall bar patterned, both width and length are 2 μm.

To determine the electronic contribution of the κ, we measured the carrier concentration of $NbSe_2$ by Hall bar measurements with prepatterned substrate (Figure 5.1a and Figure 5.1b). Both width and length are 2 μm and the mechanically exfoliated $NbSe_2$ sample is measured to be 270 nm by AFM measurements from Figure 5.1(c). The average sheet resistance from 1 μA to 500 μA is 1.145 $\Omega/\square$ and normalized to thickness returns 3.1×10^{-5} Ω cm, comparable to bulk $NbSe_2$[28] with 15×10^{-5} Ω cm. Hall coefficient is 2.47×10^{-3} $cm^3/coul$ suggesting p-type transport is also consistent with bulk data[28]. The measured Hall mobilities range from 3 to 14 cm^2/Vs, an order higher than monolayer $NbSe_2$[1]. The electron contribution for $NbSe_2$ determined by Wiedemann-Franz law is therefore 23.9 W/mK. From the electrical transport analysis , it is reasonable to state that thin film $NbSe_2$ conducts heat mostly by electrons.

APPENDIX A

ADDITIONAL POWER-DEPENDENT MEASUREMENT

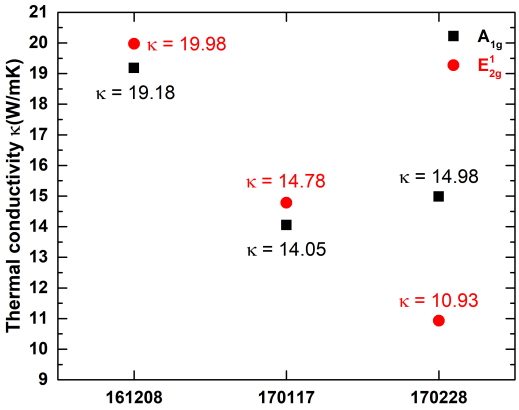

Figure A.1: κ obtained from various measurements for power-dependent Raman.Sample *161208* and *170228* does not have full coverage over the trench.

Table A.1: First-order power coefficient

Thickness	r_0 (μm)	Mode	P range (mW)	χ_P (cm^{-1}/mW)	ω_{P_0} (cm^{-1})
100 nm	0.19	E^1_{2g}	0.43~1.688	-3.13 ± 0.0191	238.999
100 nm	0.19	A_{1g}	0.43~1.688	-1.412 ± 0.029	229.35
80 nm	0.19	E^1_{2g}	0.044~0.955	-6.598 ± 0.255	238.173
80 nm	0.19	A_{1g}	0.044~0.955	-2.135 ± 0.126	229.149

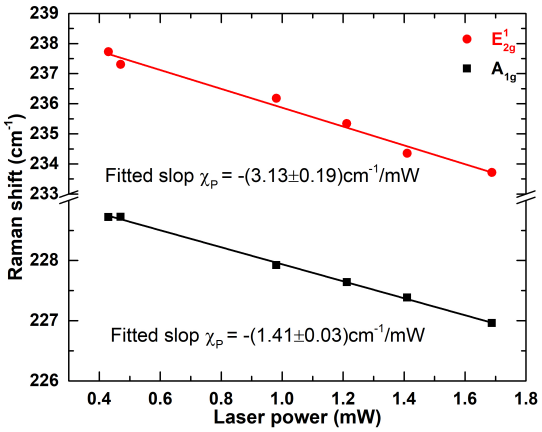

Figure A.2: Raman shift of 161208_HL_NbSe_2 (100nm) with respect to power using circular trench.

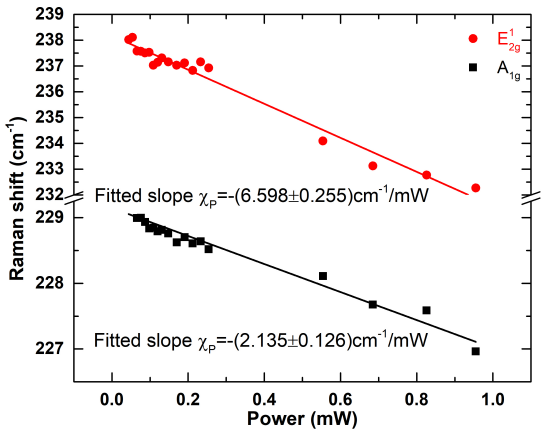

Figure A.3: Raman shift of 161208_HL_NbSe_2 (80nm) with respect to power using circular trench.

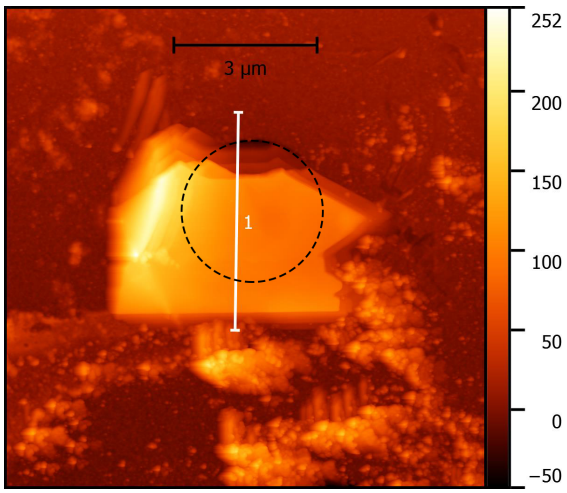

Figure A.4: AFM image of 161208_*HL_NbSe*$_2$ (100nm).

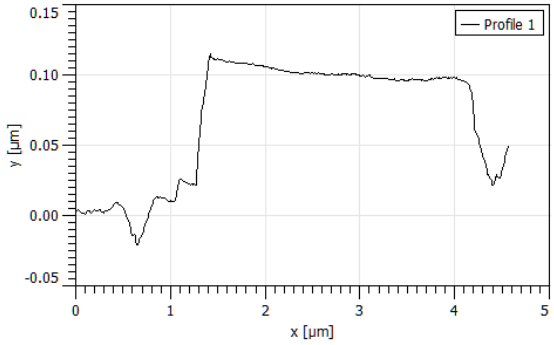

Figure A.5: Step height of 161208_*HL_NbSe*$_2$, the sample is measured to be 100 nm. Note that the trench is not fully covered.

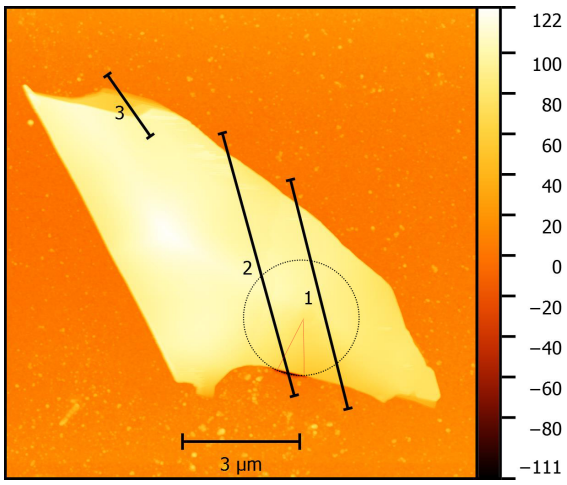

Figure A.6: AFM image of 170227_*HL_NbSe*$_2$ (80nm).

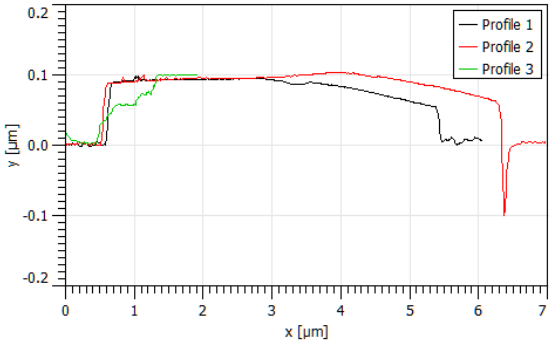

Figure A.7: Step height of 170227_*HL_NbSe*$_2$, the sample is measured to be 80 nm. Note that the trench is not fully covered.

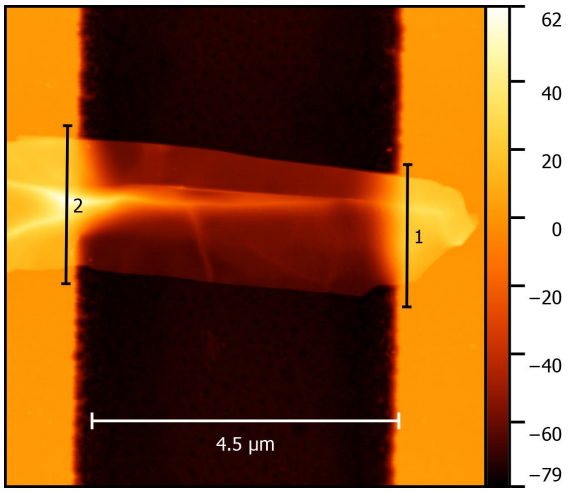

Figure A.8: AFM image of 161020_*HL_NbSe*2 (20nm). Another sample for temperature-dependent Raman.

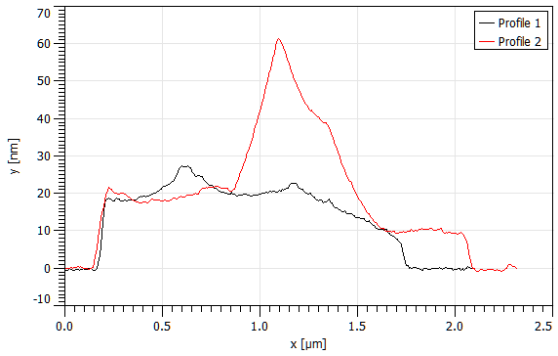

Figure A.9: Step height of 161020_*HL_NbSe*2, the sample is measured to be 20 nm.

BIBLIOGRAPHY

[1] KS Novoselov, D Jiang, F Schedin, TJ Booth, VV Khotkevich, SV Morozov, and AK Geim. Two-dimensional atomic crystals. *Proceedings of the National Academy of Sciences of the United States of America*, 102(30):10451–10453, 2005.

[2] Atsushi Koma. Van der waals epitaxya new epitaxial growth method for a highly lattice-mismatched system. *Thin Solid Films*, 216(1):72–76, 1992.

[3] E Revolinsky, GA Spiering, and DJ Beerntsen. Superconductivity in the niobium-selenium system. *Journal of Physics and Chemistry of Solids*, 26(6):1029–1034, 1965.

[4] LH Brixner. Preparation and properties of the single crystalline ab2-type selenides and tellurides of niobium, tantalum, molybdenum and tungsten. *Journal of Inorganic and Nuclear Chemistry*, 24(3):257–263, 1962.

[5] Qing Hua Wang, Kourosh Kalantar-Zadeh, Andras Kis, Jonathan N Coleman, and Michael S Strano. Electronics and optoelectronics of two-dimensional transition metal dichalcogenides. *Nature nanotechnology*, 7(11):699–712, 2012.

[6] Jarosław Judek, Arkadiusz P Gertych, Michał Świniarski, Anna Łapińska, Anna Dużyńska, and Mariusz Zdrojek. High accuracy determination of the thermal properties of supported 2d materials. *Scientific reports*, 5, 2015.

[7] TR Hart, RL Aggarwal, and Benjamin Lax. Temperature dependence of raman scattering in silicon. *Physical Review B*, 1(2):638, 1970.

[8] V Lysenko, S Perichon, B Remaki, D Barbier, and B Champagnon. Thermal conductivity of thick meso-porous silicon layers by micro-raman scattering. *Journal of Applied Physics*, 86(12):6841–6846, 1999.

[9] I Calizo, AA Balandin, W Bao, F Miao, and CN Lau. Temperature dependence of the raman spectra of graphene and graphene multilayers. *Nano letters*, 7(9):2645–2649, 2007.

[10] Harald Herchen and Mark A Cappelli. First-order raman spectrum of diamond at high temperatures. *Physical Review B*, 43(14):11740, 1991.

[11] Alexander A Balandin, Suchismita Ghosh, Wenzhong Bao, Irene Calizo,

Desalegne Teweldebrhan, Feng Miao, Chun Ning Lau, et al. Superior thermal conductivity of single-layer graphene. *Nano letters*, 8(3):902–907, 2008.

[12] Weiwei Cai, Arden L Moore, Yanwu Zhu, Xuesong Li, Shanshan Chen, Li Shi, and Rodney S Ruoff. Thermal transport in suspended and supported monolayer graphene grown by chemical vapor deposition. *Nano letters*, 10(5):1645–1651, 2010.

[13] JA Wilson and AD Yoffe. The transition metal dichalcogenides discussion and interpretation of the observed optical, electrical and structural properties. *Advances in Physics*, 18(73):193–335, 1969.

[14] David G Cahill. Thermal conductivity measurement from 30 to 750 k: the 3ω method. *Review of scientific instruments*, 61(2):802–808, 1990.

[15] Rusen Yan, Jeffrey R Simpson, Simone Bertolazzi, Jacopo Brivio, Michael Watson, Xufei Wu, Andras Kis, Tengfei Luo, Angela R Hight Walker, and Huili Grace Xing. Thermal conductivity of monolayer molybdenum disulfide obtained from temperature-dependent raman spectroscopy. *ACS nano*, 8(1):986–993, 2014.

[16] Yanlong Wang, Chunxiao Cong, Caiyu Qiu, and Ting Yu. Raman spectroscopy study of lattice vibration and crystallographic orientation of monolayer mos2 under uniaxial strain. *Small*, 9(17):2857–2861, 2013.

[17] Xian Zhang, Dezheng Sun, Yilei Li, Gwan-Hyoung Lee, Xu Cui, Daniel Chenet, Yumeng You, Tony F Heinz, and James C Hone. Measurement of lateral and interfacial thermal conductivity of single-and bilayer mos2 and mose2 using refined optothermal raman technique. *ACS applied materials & interfaces*, 7(46):25923–25929, 2015.

[18] Agnieszka Kuc, Nourdine Zibouche, and Thomas Heine. Influence of quantum confinement on the electronic structure of the transition metal sulfide t s 2. *Physical Review B*, 83(24):245213, 2011.

[19] Namphung Peimyoo, Jingzhi Shang, Weihuang Yang, Yanlong Wang, Chunxiao Cong, and Ting Yu. Thermal conductivity determination of suspended mono-and bilayer ws2 by raman spectroscopy. *Nano Research*, 8(4):1210–1221, 2015.

[20] Xian Zhang, Dezheng Sun, Yilei Li, Gwan-Hyoung Lee, Xu Cui, Daniel Chenet, Yumeng You, Tony F Heinz, and James C Hone. Measurement of

lateral and interfacial thermal conductivity of single-and bilayer mos2 and mose2 using refined optothermal raman technique. *ACS applied materials & interfaces*, 7(46):25923–25929, 2015.

[21] HR Philipp and EA Taft. Optical constants of silicon in the region 1 to 10 ev. *Physical Review*, 120(1):37, 1960.

[22] CS Wang and JM Chen. Raman spectrum of metallic layered compound nbse2. *Solid State Communications*, 14(11):1145–1148, 1974.

[23] Dattatray J Late, Sharmila N Shirodkar, Umesh V Waghmare, Vinayak P Dravid, and CNR Rao. Thermal expansion, anharmonicity and temperature-dependent raman spectra of single-and few-layer mose2 and wse2. *ChemPhysChem*, 15(8):1592–1598, 2014.

[24] Dattatray J Late, Sharmila N Shirodkar, Umesh V Waghmare, Vinayak P Dravid, and CNR Rao. Thermal expansion, anharmonicity and temperature-dependent raman spectra of single-and few-layer mose2 and wse2. *ChemPhysChem*, 15(8):1592–1598, 2014.

[25] Xiaoting Huang, Yang Gao, Tianqi Yang, Wencai Ren, Hui-Ming Cheng, and Tianshu Lai. Quantitative analysis of temperature dependence of raman shift of monolayer ws2. *Scientific Reports*, 6, 2016.

[26] RT Harley and PA Fleury. Surface brillouin scattering from layered metals and semimetals. *Journal of Physics C: Solid State Physics*, 12(22):L863, 1979.

[27] KJ Reynolds, GL Frey, and RH Friend. Solution-processed niobium diselenide as conductor and anode for polymer light-emitting diodes. *Applied physics letters*, 82(7):1123–1125, 2003.

[28] HNS Lee, H McKinzie, DS Tannhauser, and A Wold. The low-temperature transport properties of nbse2. *Journal of Applied Physics*, 40(2):602–604, 1969.